Author/s:
Song, J;Ju, Y;Amarasena, TH;Lin, Z;Mettu, S;Zhou, J;Rahim, MA;Ang, CS;Cortez-Jugo, C;Kent, SJ;Caruso, F

Title:
Influence of Poly(ethylene glycol) Molecular Architecture on Particle Assembly and Ex Vivo Particle-Immune Cell Interactions in Human Blood

Date:
2021-06-22

Citation:
Song, J., Ju, Y., Amarasena, T. H., Lin, Z., Mettu, S., Zhou, J., Rahim, M. A., Ang, C. S., Cortez-Jugo, C., Kent, S. J. & Caruso, F. (2021). Influence of Poly(ethylene glycol) Molecular Architecture on Particle Assembly and Ex Vivo Particle-Immune Cell Interactions in Human Blood. ACS Nano, 15 (6), pp.10025-10038. https://doi.org/10.1021/acsnano.1c01642.

Influence of Poly(ethylene Glycol) Molecular Architecture on Particle Assembly and *ex Vivo* Particle–Immune Cell Interactions in Human Blood

Jiaying Song,[†] Yi Ju,[†] Thakshila H. Amarasena,[‡] Zhixing Lin,[†] Srinivas Mettu,[^] Jiajing Zhou,[†] Md. Arifur Rahim,[†] Ching-Seng Ang,[#] Christina Cortez-Jugo,[†] Stephen J. Kent,[,‡] and Frank Caruso[*,†]*

[†]ARC Centre of Excellence in Convergent Bio-Nano Science and Technology, and the Department of Chemical Engineering, The University of Melbourne, Parkville, Victoria 3010, Australia

[‡]ARC Centre of Excellence in Convergent Bio-Nano Science and Technology, and Department of Microbiology and Immunology, Peter Doherty Institute for Infection and Immunity, The University of Melbourne, Parkville, Victoria 3010, Australia

[^]Department of Chemical Engineering, The University of Melbourne, Parkville, Victoria 3010, Australia

[#]Bio21 Molecular Science and Biotechnology Institute, The University of Melbourne, Parkville, Victoria 3010, Australia

Abstract

Poly(ethylene glycol) (PEG) is widely used in particle assembly to impart biocompatibility and stealth-like properties *in vivo* for diverse biomedical applications. Previous studies have examined the effect of PEG molecular weight and PEG coating density on the biological fate of various particles, however there are few studies that detail the fundamental role of PEG molecular architecture in particle engineering and bio–nano interactions. Herein, we engineered PEG particles using a mesoporous silica (MS) templating method and investigated how the PEG building block architecture impacted the physicochemical properties (*e.g.*, surface chemistry and mechanical characteristics) of the PEG particles and subsequently modulated particle–immune cell interactions in human blood. Varying the PEG architecture from 3-arm to 4-arm, 6-arm, and 8-arm generated PEG particles with a denser, stiffer structure, with increasing elastic modulus from 1.5 to 14.9 kPa, inducing an increasing level of immune cell association (from 15% for 3-arm to 45% for 8-arm) with monocytes. In contrast, the precursor PEG particles with the template intact (MS@PEG) were stiffer and generally displayed higher levels of immune cell association but showed the opposite trend—immune cell association decreased with increasing PEG arm numbers. Proteomics analysis demonstrated that the biomolecular corona that formed on the PEG particles minimally influenced particle–immune cell interactions, whereas the MS@PEG particle–cell interactions correlated with the composition of the corona that was abundant in histidine-rich glycoproteins. Our work highlights the role of PEG architecture in the design of stealth PEG-based particles, thus providing a link between the synthetic nature of particles and their biological behavior in blood.

Keywords immune cell association, human whole blood, mechanical properties, mesoporous silica, PEG particles, biomolecular corona

In recent years, a broad range of materials with specific properties and functions have been extensively investigated for particle-based drug delivery to avoid immune clearance, prolong drug circulation time, and increase target accumulation, thus exhibiting immense potential in biomedicine.[1–7] It is widely reported that the physicochemical properties of particles, including size, shape, composition, surface chemistry, and elasticity, which determine the synthetic identity of particles, can influence their behavior in a biological environment.[8–13] Specifically, this synthetic identity can influence the adsorption of biomolecules from blood and the formation of a specific biomolecular corona around the particle surface, endowing the particles with a distinct biological identity that can subsequently modulate their interactions with biointerfaces, downstream cellular responses, and their eventual biological fate.[14–19]

For optimal delivery of therapeutic cargo, extensive studies have been conducted to understand and modulate bio–nano interactions by manipulating the surface properties of particles (*e.g.*, modification with small ligands, lipids, peptides, or polymers).[20–25] PEGylation, *i.e.*, coating a material surface with a densely packed layer of poly(ethylene glycol) (PEG), is a commonly applied strategy to reduce nonspecific biological interactions.[26–28] The hydrophilic nature of PEG improves the stability of the particles and lowers their binding affinity toward biological components such as plasma proteins, which effectively shields the particles from phagocytosis, degradation, and clearance by the mononuclear phagocyte system, thereby prolonging their systemic circulation time.[29] The PEG molecular weight, PEG monodispersity, PEG coating density, and core (coated surface) properties have been reported as key factors that impact the

stealth-like properties of PEG-coated particles *in vitro* or *in vivo*.[30–33] Moreover, the benefits of PEG have inspired the development of particles composed primarily of PEG using several methods including layer-by-layer assembly, nanofabrication, and particle replication.[34–38]

Recently, we reported the engineering of PEG particles *via* mesoporous silica (MS)-templated assembly and demonstrated their potential for a range of biomedical applications, including targeted drug delivery.[39–44] The PEG particles are assembled by infiltrating PEG polymer into spherical MS templates followed by chemical cross-linking and removal of the templates to obtain replica particles with controllable particle size, tunable cross-linking density, and elasticity. The PEG molecular weight, presence or absence of the core template, and particle size significantly influenced particle association with phagocytic blood cells and biodistribution in mice.[40–42] Besides the PEG molecular weight, structural parameters of the PEG building blocks, including branching or arm architecture, are equally important to examine in the assembly of PEG particles to potentially provide further guidance on the design of PEG-based particles with tunable biological characteristics. For example, studies on branched polymers have shown that the degree of branching influences the morphology of self-assembled particle systems and the delivery efficiency of therapeutics.[45–47]

Herein, we explored how the molecular or arm architecture of PEG building blocks influences the physicochemical properties (*e.g.*, morphology and mechanical properties) of the assembled PEG particles and regulates the interactions of the assembled PEG particles with proteins and cells in human blood (Scheme 1). Four types of PEG particles were fabricated by infiltrating various multi-arm PEG building blocks (3-arm, 4-arm, 6-arm, or 8-arm) but with the same arm length into spherical MS templates followed by chemical cross-linking (Scheme 1a). The interactions between the PEG particles or the precursor particles with the MS core template intact (MS@PEG) and

human plasma proteins and immune cells were investigated by proteomics analysis and *ex vivo* human blood assays, respectively (Scheme 1b). Our results showed that PEG particles prepared from PEG building blocks with higher arm numbers exhibited denser structures with higher elastic moduli, which led to greater immune cell association when incubated in human blood independent of the composition of the biomolecular corona. In contrast, the MS@PEG particles showed decreasing immune cell association when constructed of PEG building blocks with higher arm numbers; this trend was largely influenced by the distinct composition of the biomolecular corona. This study highlights the impact of the molecular architecture of PEG building blocks on protein binding and immune cell interactions of PEG particles, thus providing an understanding of the relationships between the synthetic parameters of particles and their behavior in a complex biological environment.

Scheme 1. Schematic illustration of the assembly of PEG particles and particle–immune cell interactions in human blood.[a]

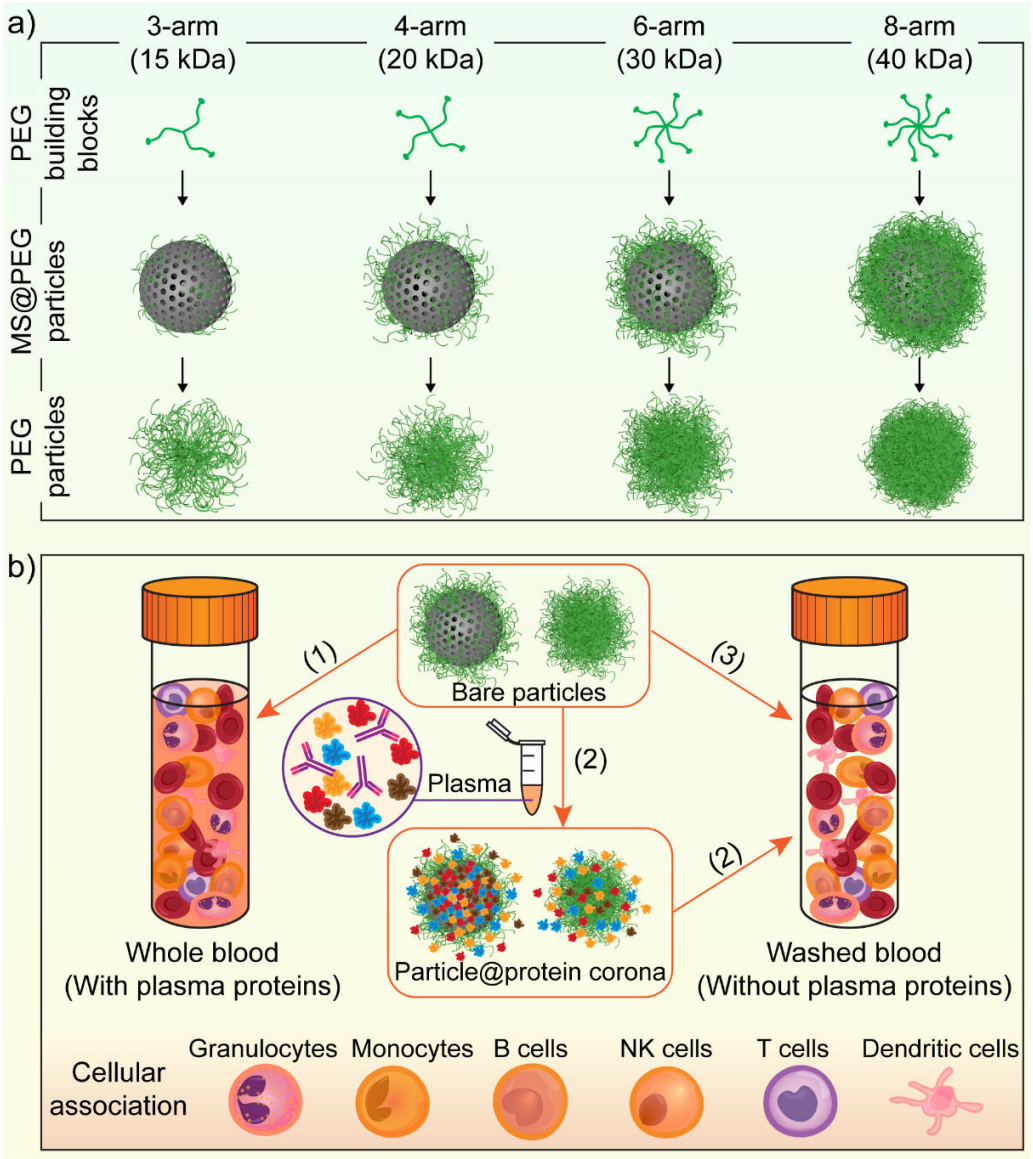

[a](a) Assembly of MS@PEG (core present) and PEG particles (core removed) using different PEG building blocks (3-arm-PEG, Mw 15 kDa; 4-arm-PEG, Mw 20 kDa; 6-arm-PEG, M_w 30 kDa; and 8-arm-PEG, M_w 40 kDa) *via* MS particle templating. (b) Human blood assays: MS@PEG particles or PEG particles are incubated in (1) human whole blood (with plasma proteins), (2) human blood plasma followed by human washed blood (without plasma proteins), that is, blood cells separated from human whole blood *via* repeated washing and centrifugation and finally suspended in DPBS, or (3) human washed blood (without plasma proteins). Particle association with human immune cells were subsequently examined.

Results and Discussions

Synthesis and Characterization of PEG Particles. PEG particles were prepared from PEG building blocks with the same arm length but different arm number (Figure S1a; amine-functionalized PEG: 3-arm-PEG-NH_2, M_w 15 kDa; 4-arm-PEG-NH_2, M_w 20 kDa; 6-arm-PEG-NH_2, M_w 30 kDa; and 8-arm-PEG-NH_2, M_w 40 kDa) *via* MS particle templating based on a modified reported method.[40] The PEG particles are respectively denoted as $PEG_{3\text{-arm}}$, $PEG_{4\text{-arm}}$, $PEG_{6\text{-arm}}$, and $PEG_{8\text{-arm}}$ particles. Although the molecular weight of the PEG building blocks increases with arm number, the change in the architecture of the building block is the main interest of this study.

The PEG particles were obtained following MS template core removal from the MS@PEG precursor particles. The MS@PEG particles were prepared by infiltration of equivalent concentrations of PEG-NH_2 from bulk solution into the pores of MS particles, PEG-NH_2 adsorption through electrostatic interactions with the surface of the particles, , followed by cross-linking with succinimidyl carboxyl methyl ester-modified PEG (Figure S1b; 8-arm-PEG-NHS, M_w 10 kDa) *via* covalent bonding. MS@PEG and PEG particles were labeled with fluorescent dye Alexa Fluor 488 (AF488) or Alexa Fluor 647 (AF647) *via* amine-succinimidyl ester cross-linking to enable particle visualization, imaging, and identification.

Figure 1 shows the morphology and structure of the $PEG_{3\text{-arm}}$, $PEG_{4\text{-arm}}$, $PEG_{6\text{-arm}}$, and $PEG_{8\text{-arm}}$ particles. As observed from the fluorescence microscopy images in Figure 1a1–d1, the PEG particles were monodisperse and displayed homogenous fluorescence in aqueous solution, with an average diameter of around 1.3 μm (Table 1). When compared with the size of the MS templates (891 ± 83 nm as determined from transmission electron microscopy (TEM) analysis, Figure S2), this size represents ~46% swelling as a result of the extensive hydration of PEG. Micrometer-sized

MS templates were used in this study for ease of PEG particle preparation and characterization, although smaller PEG particles can also be prepared using 100 nm MS templates.[40] The detailed morphology and structure of the PEG particles in the dry state were examined by TEM (Figure 1a2–d2) and atomic force microscopy (AFM; Figure 1a3–d3). The particles appeared collapsed after air-drying as a result of dehydration. $PEG_{3\text{-arm}}$ particles exhibited a loose, less dense, dendritic structure, with a thickness of 5.6 ± 1.2 nm from analysis of air-dried (*i.e.*, collapsed) particles by AFM (Table 1, Figure S3), revealing that the cross-linked PEG network was highly porous and not highly rigid. Increasing the arm number of PEG building blocks resulted in PEG particles with, generally, a denser structure that was less dendritic. Furthermore, the particle thickness (Table 1) and fluorescence intensity (Figure 2c) increased as the arm number increased, suggesting that more PEG material was cross-linked and involved in the assembly of the PEG particles. The different PEG loading amounts observed (Figure 2b) suggest that the PEG molecular architecture influences the adsorption of PEG into the pores of the MS particles, likely attributed to the distinct steric effects from the stretched PEG arms. For example, the loading amount of 8-arm-PEG-NH_2 was 192 mg g^{-1}, which is ∼3-fold higher than the loading amount of 3-arm-PEG-NH_2. The different PEG loading capacities and PEG architectures are likely to affect the subsequent cross-linking process, leading to different PEG loading densities in MS@PEG particles, and thereby distinct morphologies and structures of PEG particles after template removal. Zeta-potential measurements (Figure 2a) show that the MS@PEG particles had a less negative surface charge relative to the MS templates in phosphate buffer (pH 7.4, 5 mM) owing to the "neutral" PEG coating which could potentially arise from the zwitterionic distribution of free amine groups from PEG-NH_2 and carboxylate groups formed from the hydrolysis of the *N*-hydroxysuccinimide (NHS) ester from PEG-NHS during the cross-linking step. This neutralization effect was more obvious with

increasing arm number of the PEG building blocks owing to the higher PEG loading density and presumably different PEG conformation on the surface and within the pores masking the MS core. However, after template removal, all of the PEG particles exhibited near-neutral charge at pH 7.4 irrespective of the PEG building block architecture, due to the near-neutral charge of the PEG building blocks after cross-linking.[40]

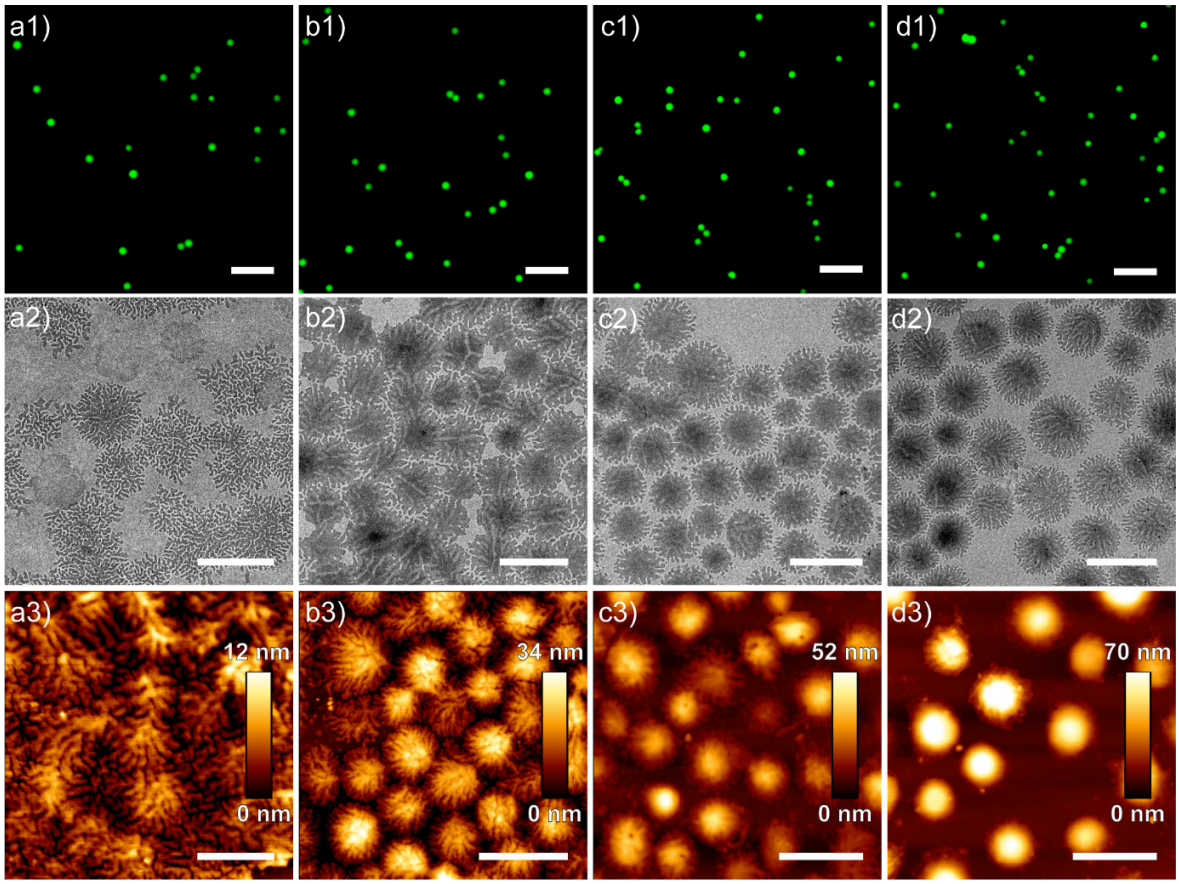

Figure 1. (a1–d1) Fluorescence microscopy, (a2–d2) TEM, and (a3–d3) AFM images of (a1–a3) $PEG_{3\text{-arm}}$ particles, (b1–b3) $PEG_{4\text{-arm}}$ particles, (c1–c3) $PEG_{6\text{-arm}}$ particles, and (d1–d3) $PEG_{8\text{-arm}}$ particles. Scale bars are 10 μm in (a1–d1) and 2 μm in (a2–d2) and (a3–d3).

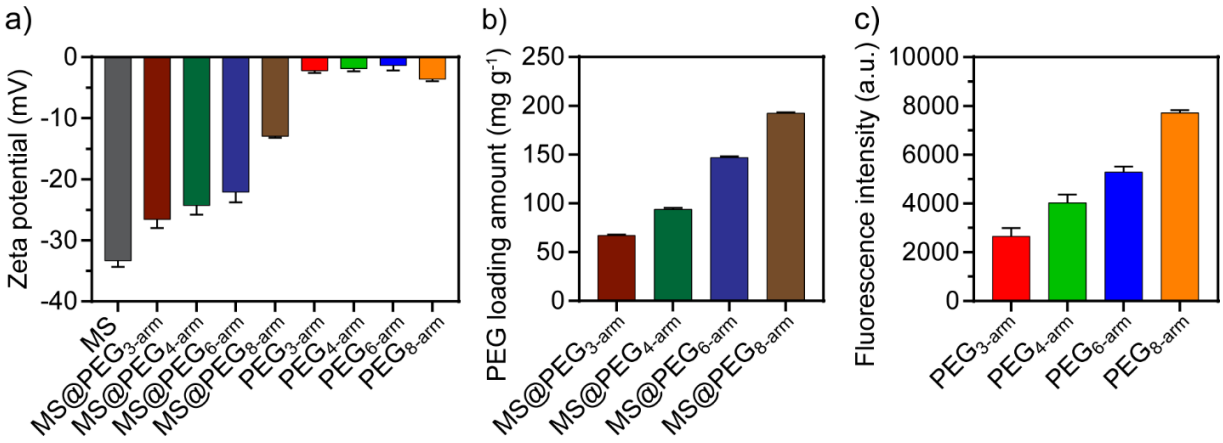

Figure 2. (a) Zeta-potential of MS, MS@PEG, and PEG particles in phosphate buffer (pH 7.4, 5 mM). (b) Loading amount of multi-arm-PEG-NH_2 (mg g^{-1}) in MS particles. (c) Fluorescence intensity of AF488-labeled PEG particles. Data are shown as the mean ± standard error of at least three independent experiments. The results of the statistical analysis are presented in Figure S4.

Table 1. Size and thickness of PEG particles

Sample	Size in aqueous solution[a] (nm)	Thickness in dry state[b] (nm)
$PEG_{3\text{-arm}}$	1316 ± 118	5.6 ± 1.2
$PEG_{4\text{-arm}}$	1310 ± 107	22.1 ± 3.4
$PEG_{6\text{-arm}}$	1313 ± 97	36.9 ± 8.3
$PEG_{8\text{-arm}}$	1333 ± 40	55.9 ± 4.1

[a]Determined from fluorescence microscopy images using ImageJ software. The full width at half maximum of the fluorescence profile across the particles was considered as the particle diameter. The data are shown as the mean ± standard deviation, and 40 particles were analyzed for each sample.

[b]Determined from the distance between the highest point on the particle (air-dried) and the substrate surface using AFM. The data are shown as the mean ± standard deviation, and 15 particles were analyzed for each sample.

Mechanical Properties of PEG Particles. Given the distinct particle structures obtained from using the PEG building blocks with different architectures, the mechanical properties of the PEG particles were evaluated by colloidal-probe atomic force microscopy (CP-AFM) technique

(Figures 3a and S5). The AFM probe was slowly lowered onto the individual immobilized PEG particles in aqueous solution to perform the force measurements. Force–deformation (F–δ) curves (Figure 3b) were obtained from the raw AFM voltage–displacement data processed using JPK data processing software (v.4.4.29). The Young's modulus value of the PEG particles was calculated from the linear range (δ from 0 to 200 nm) of the F–$\delta^{3/2}$ curves using Hertz theory (as described in *Mechanical Property Measurements and Analysis* in *Methods*). As shown in Figure 3c, the Young's modulus of the PEG particles generally increased with increasing arm number of the PEG building block, from 1.5 kPa for $PEG_{3\text{-arm}}$ particles to 14.9 kPa for the $PEG_{8\text{-arm}}$ particles. As the particles were formed with the same material and had similar sizes in aqueous solution, the elastic modulus of the particles was mostly governed by the material density within the cross-linked structure. $PEG_{8\text{-arm}}$ particles had the highest Young's modulus value among the four types of PEG particles studied, which is consistent with the highest particle density observed from the TEM and AFM images in Figure 1. Although not specially studied here, an alternative approach to increase the stiffness of the PEG particles may be to vary the concentration of $PEG_{8\text{-arm}}$ cross-linker.[39] Here, we show that increasing the arm number of the PEG building block results in higher cross-linking density and stiffness. For the MS@PEG particles, as the rigid MS template plays a dominant role in the particle structure (Figure S6), they are expected to display comparable stiffness properties, with considerably higher Young's moduli than those displayed by the PEG particles.[48]

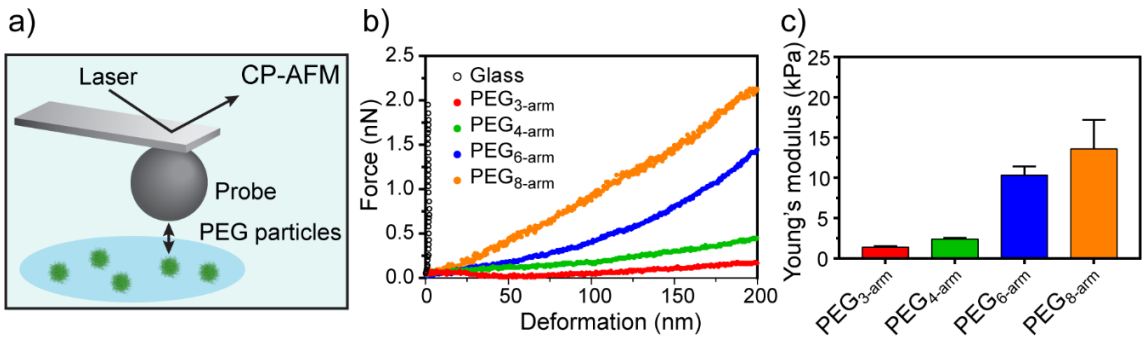

Figure 3. (a) Schematic illustration of the elastic modulus measurements performed on the PEG particles by CP-AFM. (b) Force–deformation (F–δ) curves of $PEG_{3\text{-arm}}$, $PEG_{4\text{-arm}}$, $PEG_{6\text{-arm}}$, and $PEG_{8\text{-arm}}$ particles. The F–δ curve of a glass substrate is also shown for calibration. (c) Young's modulus values of the PEG particles derived from the F–δ analysis.

Association of PEG Particles with Macrophages or Human Immune Cells. To investigate the effect of PEG building block architecture on the stealth-like properties of the assembled PEG particles, the cellular association of the MS@PEG and PEG particles was first measured using a commonly employed murine macrophage-like cell line RAW264.7. The PEG particles displayed low cellular association (<5%) regardless of the PEG building block architecture and incubation time (Figure S7), confirming their stealth-like property. Increasing the PEG particle dosage (particle-to-cell ratio from 100:1 to 1000:1) resulted in a slightly higher cell association (Figure S7b), with the $PEG_{8\text{-arm}}$ particles exhibiting the highest association (15%). In contrast, a significantly higher cellular association was observed for all of the MS@PEG particles (>90% after 12 h of incubation) than that observed for the corresponding PEG particles (Figure S7a). Confocal microscopy images were consistent with the flow cytometry results, with the PEG particles associating with RAW264.7 cells in low numbers, whereas more than 90% of cells internalized MS@PEG particles (Figure S8).

However, employing a single-model cell line, wherein the cells are cultured under non-physiological conditions and the limited presence of biological components, is not representative of the cells in complex biological environments.[49] Many particles fail to fulfil their designed functions following intravenous administration as they are rapidly recognized and sequestered by the mononuclear phagocyte system, which is responsible for the clearance of dead cells, pathogens, and foreign substances from the blood circulation system.[9,50] In contrast, human whole blood, a

highly complex biological system consisting of red blood cells, immune cells (including phagocytic blood cells), and a variety of biomolecules (such as plasma proteins and antibodies), is considered to be a more physiologically relevant model than a mono-cultured cell line to study bio–nano interactions and predict particle behaviors *in vivo*.[51,52] Herein, AF647-labeled MS@PEG or PEG particles were incubated in fresh healthy human whole blood at varying particle-to-cell ratios for 1 h at 37 °C to investigate the particle–immune cell interactions. The major human immune cells in blood (granulocytes, monocytes, B cells, NK cells, T cells, and dendritic cells) were labeled with a fluorescent antibody cocktail for the identification of different cell populations. Cellular association was measured by flow cytometry and analyzed using a previously established method (Figure S9)[53] and Figure S10, which shows distinct AF647+ and AF647− cell populations, demonstrated that PEG particle fluorescence intensity has little influence in the interpretation of the flow cytometry results.

Consistent with the results derived from the RAW264.7 cell assay, the MS@PEG particles showed notably higher association with phagocytes (granulocytes and monocytes) and B cells compared with the corresponding PEG particles at the same particle-to-cell ratio (50:1) (Figure 4). The higher cellular association behavior displayed by the MS@PEG particles in comparison with the PEG particles may be due to their rigid structure and negatively charged surface that may adsorb immune-related biomolecules by electrostatic interactions.[12,21,54] At the lower particle-to-cell ratios (20:1, 10:1, and 5:1), the MS@PEG particles displayed consistently lower immune cell association, which decreased as the PEG arm number increased (Figure 4a). For example, the association of the MS@PEG$_{8\text{-arm}}$ particles with granulocytes upon incubation at a particle-to-cell ratio of 20:1 was 4%, which is only ~5% of the association of the MS@PEG$_{3\text{-arm}}$ particles. This lower cell association is most likely due to the higher mass of PEG protective layer on the MS core

when loading PEG building blocks with higher arm numbers (Figure 2b) and the resulting less negatively charged surface of MS@PEG$_{8\text{-arm}}$ particles (Figure 2a).

The opposite trend was observed for the PEG particles (Figure 4b). The PEG particles prepared from PEG building blocks with higher arm numbers induced higher phagocyte and B cell association and this was more pronounced at higher particle dosages. For example, the association of PEG$_{8\text{-arm}}$ particles with granulocytes or monocytes was 2–4 fold higher than that of PEG$_{3\text{-arm}}$ particles. As these PEG particles are made of the same material with a comparable surface charge (~0 mV), the differences in cellular association largely result from the differences in particle structure, morphology, and elasticity.[12,55–58] Softer and more dendritic PEG particles (*e.g.*, PEG$_{3\text{-arm}}$ particles) exhibited stronger resistance against immune cell association than their stiffer and denser counterparts (*e.g.*, PEG$_{8\text{-arm}}$ particles) and are hence expected to achieve better stealth performance and longer systemic circulation *in vivo*. While previous findings have shown that PEG particles prepared from higher molecular weight PEG (fixed arm number but longer arms) exhibit lower immune cell association,[40] our results show that the molecular architecture of the PEG building blocks, such as the arm number, is also an important factor to consider when designing stealth PEG-based particle systems, as it can influence the physicochemical properties (*e.g.*, morphology and mechanical property) of the assembled PEG particles. Notably, as the results demonstrate, such architectural effects of PEG building blocks on particle behaviors can be completely different depending on the particle type (*e.g.*, PEG-coated particles or pure PEG particles).

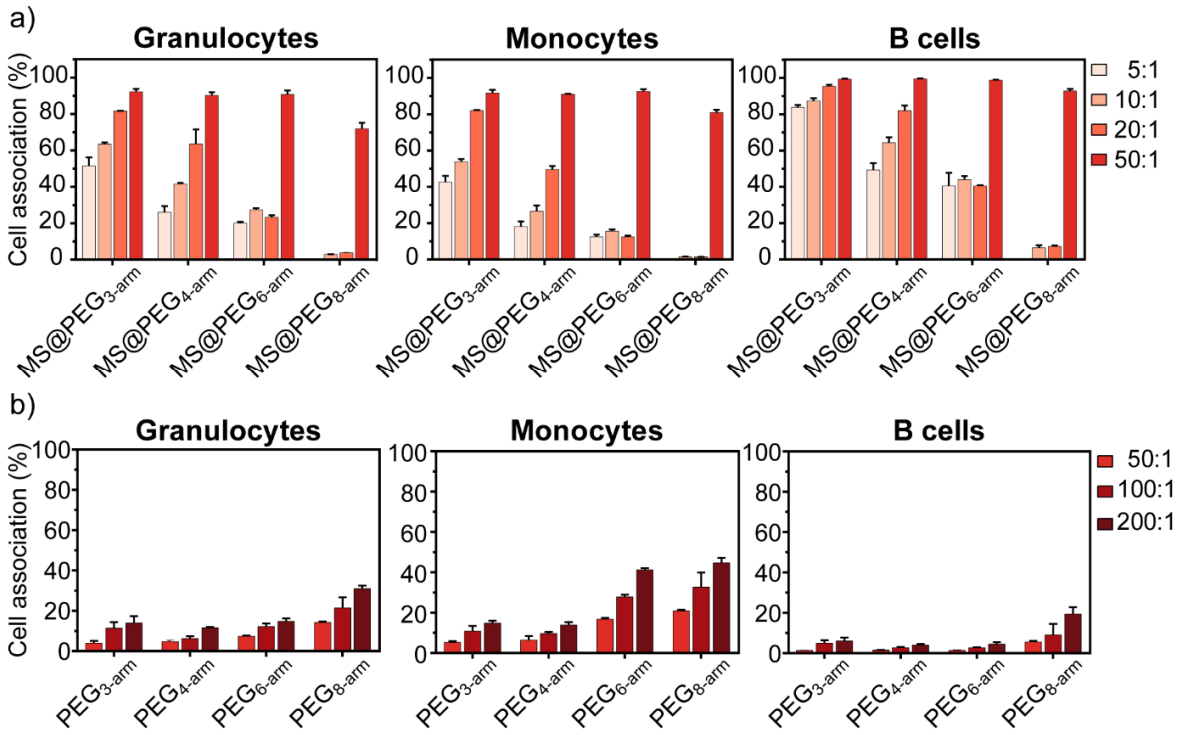

Figure 4. Cellular association of (a) MS@PEG particles and (b) PEG particles with granulocytes, monocytes, and B cells after incubation in human whole blood for 1 h at 37 °C at varying particle-to-cell ratios. Cell association (%) refers to the proportion of cells with positive fluorescence, above background, derived from AF647-labeled particles. Data are shown as the mean ± standard error of three independent experiments, with at least 100 000 leukocytes analyzed in each individual experiment. The results of the statistical analysis are presented in Figures S11 and S12. Cellular association with the other blood cell populations, *i.e.*, NK cells, T cells, and dendritic cells, is shown in Figure S13.

Role of the Biomolecular Corona in Particle–Immune Cell Interactions. Nanoengineered particles will interact with a variety of biological components when entering physiological environments, resulting in the distinct adsorption of biomolecules and the formation of a specific biomolecular corona, which is generally composed of an inner tightly bound layer termed the “hard

corona" and an outer loosely associated layer termed the "soft corona" (which can be removed by washing).[16,59] To elucidate how the synthetic identity of particles modulates their behaviors in biological environments, it is essential to understand the role of the biomolecular corona. As shown in Figure S14, incubating the particles in blood plasma resulted in a slight increase of negative charge for all of the PEG particles and a "normalization" of zeta-potential to –20 mV for the MS@PEG$_{3\text{-arm}}$, MS@PEG$_{4\text{-arm}}$, and MS@PEG$_{6\text{-arm}}$ particles. In contrast, the surface charge of the MS@PEG$_{8\text{-arm}}$ particles remained unchanged (–12 mV). We then examined the cellular association of the MS@PEG and PEG particles incubated under different conditions: (1) human whole blood; (2) human blood plasma followed by washed blood; and (3) human washed blood, where either "hard" and "soft" corona (1 and 2) or "no" corona (3) was formed (Scheme 1b). Condition (1) refers to particles treated with human whole blood where both plasma biomolecules and blood cells are present. Condition (2) refers to particles preincubated in blood plasma to allow the formation of a biomolecular corona on the particle surface, followed by incubation with blood cells that had been separated from human whole blood *via* repeated washing and centrifugation (termed washed blood). Condition (3) refers to particles incubated in washed blood directly where only blood cells are present without plasma biomolecules. Owing to the stealth-like properties of the PEG particles, a much higher particle-to-cell ratio (100:1) was used to assess the association of the PEG particles with blood cells than that used (10:1) for the MS@PEG particles to discriminate any association between the different PEG particles.

As shown in Figure 5a, the cellular association of the MS@PEG particles incubated in washed blood directly (3) was considerably reduced to extremely low levels (less than 20%) in contrast to the results observed upon incubation in whole blood (1). This result indicates that immune recognition and cell association of the MS@PEG particles are dependent on a biomolecular

corona, most likely through the interactions between the corona proteins and the receptors on the cell membrane. This finding is further supported by the results obtained upon preincubating particles in blood plasma, followed by incubating with washed blood (2), where cellular association to high levels was restored. Furthermore, despite the low levels of cellular association in the absence of plasma biomolecules, there were still measurable differences between the MS@PEG$_{8\text{-arm}}$ particles and the other MS@PEG particles (Figure S15). These differences suggest that besides the impact caused by a biomolecular corona, the synthetic properties of a particle can directly influence its interactions with immune cells presumably through a serum-independent mechanism.

In contrast, no marked differences were observed between the cellular association of the PEG particles with (2) and without (3) plasma biomolecules (Figures 5b and S16). The environmental biomolecules may have minimally altered the PEG particle identity and do not significantly contribute to the immune cell association of the PEG particles. We can hypothesize that the predominant cellular association of PEG particles is serum-independent and may rely on the direct interactions (*e.g.*, hydrogen bonding) between the PEG chains and the biomolecules (*e.g.*, proteins and lipids) on the cell membrane rather than protein–receptor interactions.[9,60] The pronounced cell association of PEG$_{8\text{-arm}}$ particles in comparison with the other PEG particles suggests that the synthetic properties of PEG particles, especially the particle structure and elasticity, can directly influence their interactions with cells.

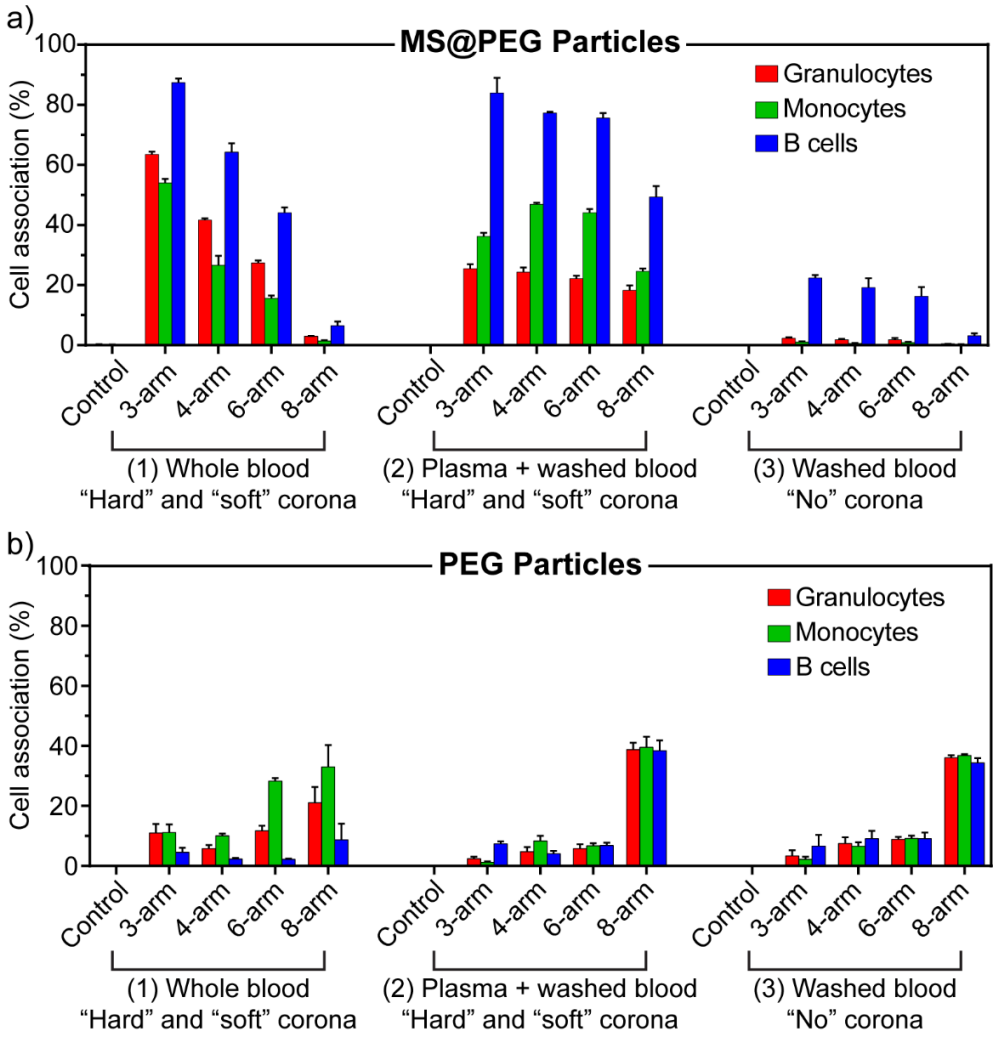

Figure 5. Association of (a) MS@PEG and (b) PEG particles with granulocytes, monocytes, and B cells after incubation in (1) human whole blood, (2) blood plasma followed by human washed blood, or (3) human washed blood. Based on the different incubation conditions, either a "hard" and "soft" corona (1 and 2) or "no" corona (3) was formed on the particles. The particle-to-cell ratio was set at 10:1 for the MS@PEG particles and 100:1 for the PEG particles. Cell association (%) refers to the proportion of cells with positive fluorescence, above background, derived from AF647-labeled particles. Data are shown as the mean ± standard error of three independent

experiments, with at least 100 000 leukocytes analyzed in each individual experiment. Control refers to the cell populations without particle treatment in the incubation medium.

Proteomics Analysis of the Biomolecular Corona. The differences in immune cell association across the particles with and without plasma strongly suggest that the plasma biomolecular corona plays a critical role in regulating particle–immune cell interactions. Therefore, proteins eluted from the biomolecular coronas on the different MS@PEG and PEG particles were analyzed by sodium dodecyl sulfate-polyacrylamide gel electrophoresis (SDS-PAGE) (Figure S17). A dense band between 64 and 98 kDa corresponding to histidine-rich glycoproteins was observed for all the MS@PEG particles, whereas negligible protein adsorption was detected for the PEG particles owing to the absence of bands in the gel. To obtain insight into the relationships between particle physicochemical properties, formation of biomolecular corona, and particle–immune cell interactions, proteomics analysis of the biomolecular corona was conducted by label-free liquid chromatography-tandem mass spectrometry (LC-MS/MS).

The identification and relative quantification of the adsorbed proteins on the different MS@PEG and PEG particles are shown in Figures 6 and 7. The MS@PEG particles adsorbed 4–8 times more proteins than the PEG particles (Figure 6b), in agreement with the SDS-PAGE data (Figure S17). However, no significant differences in total protein adsorption were observed for the MS@PEG or PEG particles with varying PEG building block architecture (Figure S18), which suggests that the total amount of corona proteins may not necessarily determine the particle–immune cell interactions. Therefore, the corona composition was subsequently analyzed. As shown in Figure 6a, the MS@PEG and PEG particles displayed different patterns of protein adsorption. For example, histidine-rich glycoprotein (HRG) was the most predominant corona protein on the MS@PEG particles, with the relative abundance varying from 59% to 85% (calculated from the

intensity-based absolute quantification (iBAQ) values; see *Proteomics Analysis by Mass Spectrometry* in *Methods*) depending on the PEG building block architecture (consistent with the SDS-PAGE results, Figure S17). In contrast, HRG only made up ~0.2% of the corona proteins on the PEG particles. The major proteins adsorbed on the PEG particles (*e.g.*, albumin (ALB) and actin, cytoplasmic 1 (ACTB)) were detected in relatively low abundances on the MS@PEG particles. The corona proteins were classified according to their molecular weight (Figure 6c), isoelectric point (pI) (Figure 6d), and biological function (Figure 7) based on the UniProt human database. Generally, the PEG particles prepared from different PEG building blocks displayed similar protein profiles (in terms of the previously listed classifications), whereas the MS@PEG particles displayed different distributions. Intermediate molecular weight proteins (50–80 kDa) constitute the majority of corona proteins for the MS@PEG particles (increasing from 72% for MS@PEG$_{3\text{-arm}}$ up to 95% for MS@PEG$_{8\text{-arm}}$ particles), whereas lower molecular weight proteins (<50 kDa, ~60%) were preferentially adsorbed on the PEG particles (Figure 6c). Proteins exhibiting a neutral or negative charge at pH 7.4 were mainly adsorbed on both the negatively charged MS@PEG particles and neutral PEG particles (Figure 6d), indicating that the adsorption of proteins is not merely driven by electrostatic interactions. Complex interactions including hydrogen bonding, hydrophobic interactions, and van der Waals forces may contribute to the formation of a biomolecular corona.[61] It is noted that the relative abundance of the functional proteins involved in specific physiological processes (*e.g.*, immunoglobulins, apolipoproteins, acute phase proteins, and coagulation proteins) varied with the PEG building block architecture for MS@PEG particles (Figure 7a–h). The markedly increased enrichment of the predominant coagulation proteins (mostly HRG) from MS@PEG$_{3\text{-arm}}$ to MS@PEG$_{4\text{-arm}}$, MS@PEG$_{6\text{-arm}}$, and MS@PEG$_{8\text{-arm}}$ particles (Figure 7e) may be responsible for the decreased relative abundance of

the other common proteins (*e.g.*, immunoglobulins, apolipoproteins, tissue leakage proteins, and acute phase proteins) by competing for the binding sites on the particle surface.[62–64] The gradual decrease in the relative abundance of immunoglobulins (from 2.2% for MS@PEG$_{3\text{-arm}}$ to 0.8% for MS@PEG$_{8\text{-arm}}$, Figure 7b) may contribute to the reduced immune cell association of the MS@PEG particles (with a significant positive correlation between monocyte uptake and immunoglobulin abundance as shown in Table 2), as the opsonins (*e.g.*, immunoglobulin G (IgG)) were found to promote immune recognition and phagocytosis in previous studies.[16] In contrast, for the PEG particles, although varying the PEG building block architecture resulted in a few changes in the corona composition (Figure 7i–p), such variations were not as marked or as clearly associated in a regular manner with the PEG arm number. Notably, no significant correlation was observed between the abundance of the functional corona proteins and immune cell association of the PEG particles (p-value > 0.05, Table 2), indicating that the association of the PEG particles with immune cells may not predominantly rely on plasma proteins.

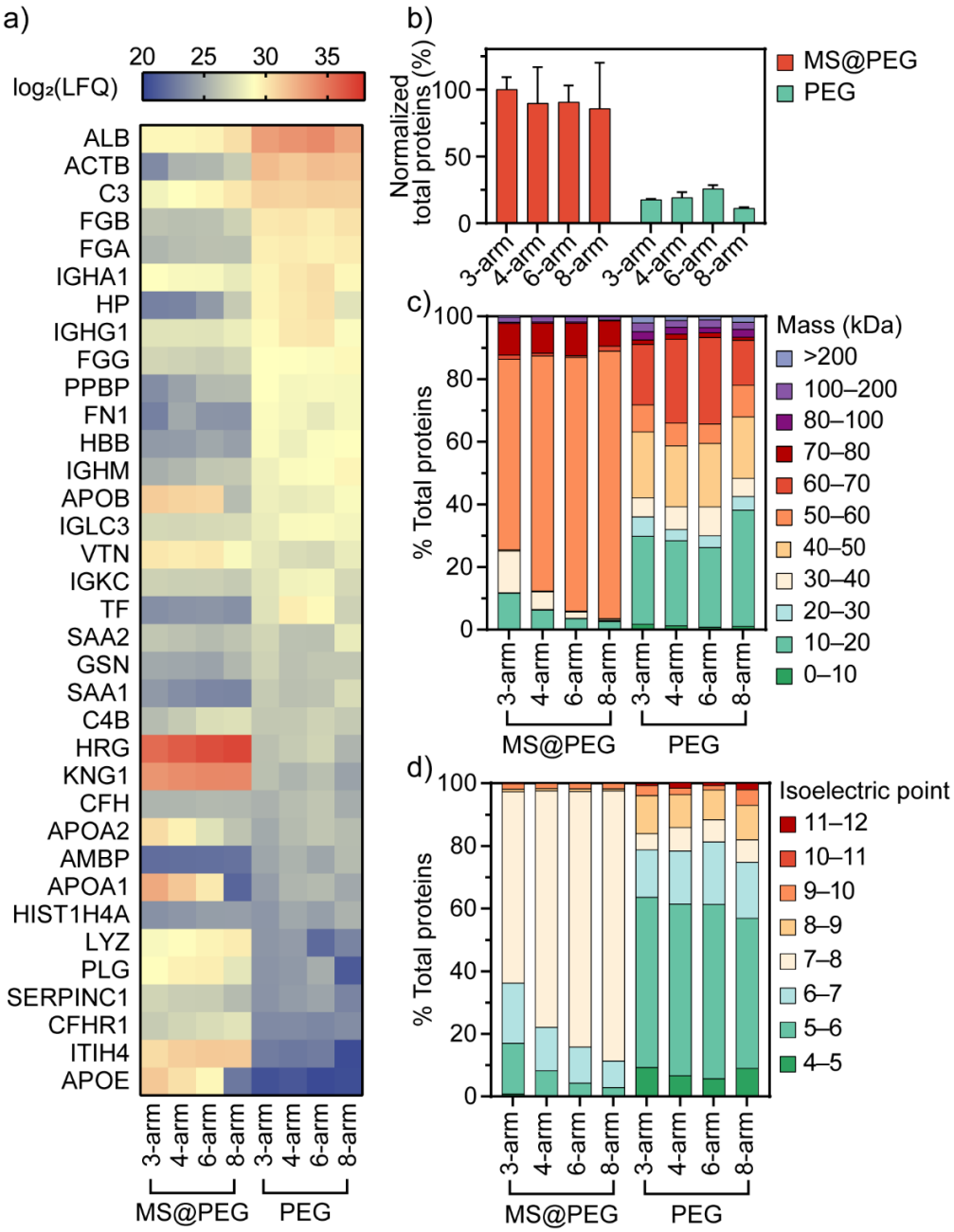

Figure 6. Identification and relative quantification of the proteins adsorbed on the MS@PEG and PEG particles characterized by label-free LC-MS/MS. (a) Heat map representation of the top 35 proteins adsorbed on the MS@PEG and PEG particles. The relative abundance is shown in blue–yellow–red colors corresponding to the values of $\log_2$ transformed intensities of label-free quantification (LFQ) ($\log_2$(LFQ)). Full lists are shown in Table S1. (b) Total protein adsorption on

MS@PEG and PEG particles expressed as a percentage relative to that on MS@PEG$_{3\text{-arm}}$ particles (normalized as 100%). Classification of the adsorbed proteins according to their (c) molecular weight and (d) isoelectric point. The protein contents (mol% of total proteins) are calculated from the iBAQ values. In (a), (c), and (d), the data are the average of three independent replicates. In (b), the data are shown as the mean ± standard deviation (n = 3).

Table 2. Pearson correlation between the functional corona proteins identified on MS@PEG and PEG particles and particle association with monocytes (at particle-to-cell ratios of 20:1 for MS@PEG particles and 200:1 for PEG particles)

Proteins	MS@PEG particles		PEG particles	
	Correlation coefficient, r	p-Value	Correlation coefficient, r	p-Value
Complement	–0.7385	0.2615	–0.5145	0.4855
Apolipoproteins	0.9812	0.0188	0.6834	0.3166
Immunoglobulins	0.9709	0.0291	0.2078	0.7922
Histidine-rich glycoproteins	–0.9779	0.0221	–0.1634	0.8366

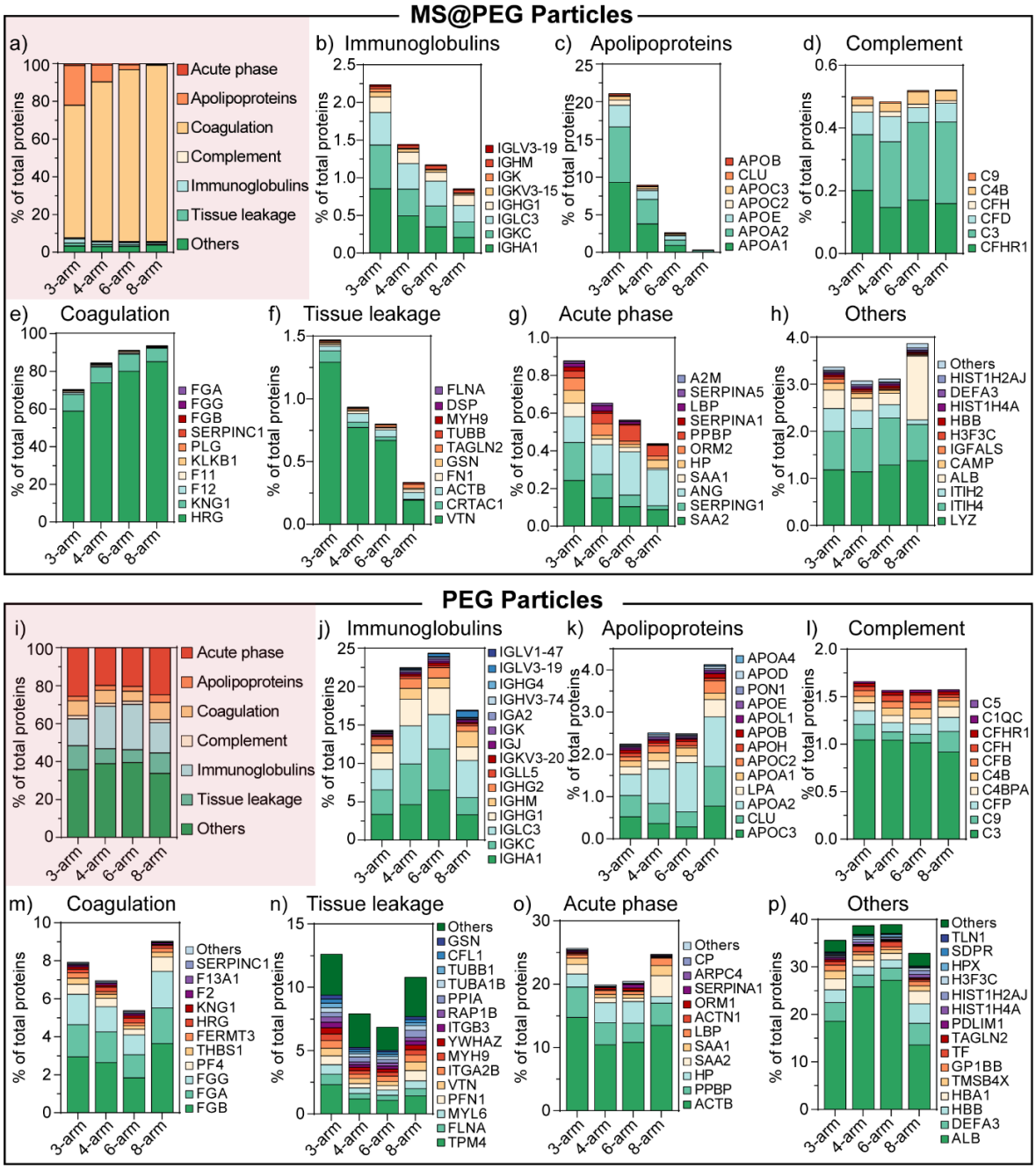

Figure 7. Classification of the corona proteins identified on the MS@PEG and PEG particles according to their biological function in the blood system. The protein contents (mol% of total proteins) are calculated from the iBAQ values. The data are the average of three independent replicates. Full lists are shown in Tables S2 and S3.

Conclusions

The effect of the PEG building block architecture on the assembly of PEG replica particles and their bio–nano interactions in human blood was examined by varying the PEG building block architecture from 3-arm to 4-arm, 6-arm, and 8-arm. Increasing the arm number of the PEG building blocks resulted in higher PEG loading amounts in the precursor MS@PEG particles, which translated to denser and stiffer PEG replica particles after template removal—the Young's modulus increased from 1.5 kPa for the $PEG_{3\text{-arm}}$ particles to 14.9 kPa for the $PEG_{8\text{-arm}}$ particles. When incubated in human whole blood, the PEG particles assembled from PEG building blocks with higher arm numbers generally exhibited greater cellular association because the particles were denser and stiffer. The opposite trend was observed for the MS@PEG particles (lower cellular association was observed with higher arm numbers), potentially because of a denser PEG coating on the MS@PEG particles with a less negative surface charge at the higher arm numbers. Examination of the biomolecular corona confirmed that the PEG particles are less fouling than their precursor particles, with the biomolecular corona playing a limited role in particle–immune cell interactions. The biomolecular corona, however, significantly influenced the association of the MS@PEG particles with immune cells—binding highly correlated with the presence and composition of the biomolecular corona, which was abundant in histidine-rich glycoproteins that could compete with other functional proteins (*e.g.*, immunoglobulins) and thus regulate immune cell interactions. Our findings suggest that the physicochemical properties of the PEG particles obtained from varying the molecular architecture of the PEG building blocks are dominant factors in the interaction of PEG particles with immune cells. Our study highlights the important role of polymer architecture in the design of stealth PEG-based particle systems for biomedical applications and demonstrates how the synthetic identity of particles can be engineered by tuning

the structural parameters of building blocks to control the biological identity of the particles and regulate their immune cell response in physiological environments. The study also highlights the role of surface charge, influenced by the PEG loading amount, on MS particles. Although the surface charge on MS@PEG particles had little influence on the amount of total protein adsorbed from human blood, it did impact the composition of the protein corona, which could be exploited to control immune cell interactions.

Methods

Materials. Tetraethyl orthosilicate (TEOS), cetyltrimethylammonium bromide (CTAB), poly(acrylic acid) (PAA, M_w ~250 kDa, 35 wt.% solution in water), ammonium hydroxide solution ($NH_3 \cdot H_2O$, 28–30%), sodium phosphate dibasic (Na_2HPO_4), hydrofluoric acid (HF, 48 wt.%), ammonium fluoride (NH_4F), anhydrous dimethyl sulfoxide (DMSO), Dulbecco's phosphate-buffered saline (DPBS), paraformaldehyde, formaldehyde, ethylenediaminetetraacetic acid (EDTA), bovine serum albumin (BSA), fluorescamine, poly(ethyleneimine) (PEI), acetonitrile (CH_3CN), tetraethylammonium bromide (TEAB), tris(2-carboxyethyl)phosphine hydrochloride (TCEP), trifluoroacetic acid (TFA), trifluoroethanol (TFE), iodoacetamide (IAM), trypsin from porcine pancreas (proteomics grade), and formic acid were obtained from Sigma-Aldrich (Australia). Amine-functionalized PEG: 3-arm-PEG-NH_2 (M_w 15 kDa), 4-arm-PEG-NH_2 (M_w 20 kDa), 6-arm-PEG-NH_2 (M_w 30 kDa), and 8-arm-PEG-NH_2 (M_w 40 kDa) were obtained from JenKem Technology USA Inc. (China). 8-Arm-PEG-NHS (hexaglycerol core, M_w 10 kDa) was purchased from Creative PEGWorks (USA). Dulbecco's modified Eagle's medium, Alexa Fluor 488 carboxylic acid succinimidyl ester (AF488), Alexa Fluor 647 carboxylic acid succinimidyl ester (AF647), RPMI-1640 medium, fetal bovine serum (FBS), wheat germ agglutinin Alexa Fluor 594 conjugate (WGA-594), Hoechst 33342, NuPAGE LDS sample buffer, NuPAGE sample

reducing agent, SeeBlue Plus2 pre-stained protein standard, and SimplyBlue safe stain were purchased from Life Technologies (Australia). BioRad 4–20% Mini-PROTEAN TGX gel and Tris/glycine/SDS running buffer were purchased from BioRad (CA, USA). The antibodies CD66b BV421 (G10F5), CD19 BUV395 (SJ25C1), CD3 AF700 (SP34-2), CD14 APC-H7 (MΦP9), CD56 PE (B159), and HLA-DR PE-CF594 (G46-6) were purchased from BD Biosciences. The antibody lineage cocktail 1 fluorescein isothiocyanate (Lin-1 FITC) was obtained from BioLegend (USA). High-purity water used in all experiments was obtained from a three-stage Millipore Milli-Q plus 185 purification system (Millipore Corporation) with a resistivity greater than 18.2 MΩ cm.

Synthesis of MS Particles. MS particles were synthesized according to a previously reported method.[40] Briefly, 1.1 g of CTAB was dissolved in 50 mL of water under constant stirring. Then, 4.28 g of PAA solution (35 wt.% in water) was added to the above solution. When the solution turned clear after *ca.* 20 min, 3.5 mL of ammonium hydroxide solution (28–30%) was added with vigorous stirring. Then, 4.46 mL of TEOS was added to the above milky suspension after stirring for 20 min. The suspension was further stirred for 15 min and finally placed into a Teflon-sealed autoclave at 90 °C for 48 h. After washing with water and ethanol, followed by drying at 80 °C, the synthesized MS particles were calcined at 550 °C in air for 30 h (heating ramp of 5 °C min^{-1}) to remove the organic materials.

Synthesis of MS@PEG and PEG Particles. MS@PEG and PEG particles were synthesized according to a modified published method.[40] For instance, to prepare MS@$PEG_{3\text{-arm}}$ and $PEG_{3\text{-arm}}$ particles, 480 μL of 3-arm-PEG-NH_2 solution (5 mg mL^{-1} in 100 mM, pH 8.0 phosphate buffer) was added to ~6 mg of MS particles for overnight incubation with constant shaking. 3-Arm-PEG-NH_2 was infiltrated into the pores of the MS particles driven by electrostatic interactions. The

particles were then washed with phosphate buffer three times to remove excess polymer. To determine the amount of 3-arm-PEG-NH_2 loaded in the MS particles, the supernatant after each wash was collected and the concentration of 3-arm-PEG-NH_2 in the supernatant was determined by a fluorescamine assay (Sigma-Aldrich, Australia) according to the manufacturer's protocol. The fluorescence intensity of the samples (λ_{ex} = 400 nm; λ_{em} = 490 nm) measured by an Infinite M200 microplate reader (Tecan, Switzerland) was converted to PEG concentration based on a standard curve generated with serial dilutions of 3-arm-PEG-NH_2 solution (0–1.0 mg mL^{-1}). The amount of PEG-NH_2 loaded in the MS particles (q; mg g^{-1}) was calculated according to Equation (1):

$$q = \frac{CV - C'V'}{m} \quad (1)$$

where C is the concentration of PEG-NH_2 in the stock solution (mg mL^{-1}), C' is the concentration of PEG-NH_2 in the supernatant (mg mL^{-1}), V is the volume of the stock solution (mL), V' is the volume of supernatant (mL), and m is the mass of the MS particles (g).

The PEG-loaded MS particles were subsequently incubated in 400 μL of 8-arm-PEG-NHS solution (2 mg mL^{-1} in phosphate buffer) for 2 h for cross-linking. The MS@$PEG_{3\text{-arm}}$ particles were labeled with AF488 or AF647 (5 μL, 1 mg mL^{-1} in anhydrous DMSO) during the cross-linking step. The resultant particles were washed three times with water to remove unreacted cross-linker and dye. The $PEG_{3\text{-arm}}$ particles were obtained by dissolving the MS templates using a 2 M HF/8 M NH_4F solution (pH ~5). *Caution! HF is highly toxic and extreme care should be taken during handling.* The resultant $PEG_{3\text{-arm}}$ particles were washed three times with water and resuspended in water for further experiments.

For the preparation of MS@PEG$_{4\text{-arm}}$ or PEG$_{4\text{-arm}}$, MS@PEG$_{6\text{-arm}}$ or PEG$_{6\text{-arm}}$, and MS@PEG$_{8\text{-arm}}$ or PEG$_{8\text{-arm}}$ particles, respectively, 4-arm-PEG-NH_2, 6-arm-PEG-NH_2, and 8-arm-PEG-NH_2 were used as the building blocks.

Characterization of the Synthesized Particles. Fluorescence microscopy images were taken with an Olympus IX71 inverted fluorescence microscope equipped with a differential interference contrast (DIC) slider (U-DICT, Olympus), filter sets for fluorescence imaging, and a 100× oil immersion objective (Olympus UPFL20/0.5NA, W.D. 1.6). TEM images were taken with an FEI Tecnai TF20 instrument operating at 80 kV for the PEG particles and 120 kV for the MS particles. The TEM samples were prepared by placing a drop of an aqueous particle suspension onto plasma-treated formvar-coated copper grids and subsequent drying in air. AFM images were acquired on a NanoWizard II atomic force microscope (JPK Instruments, Berlin, Germany). An aqueous suspension of the particles was placed onto Piranha-precleaned glass slides and dried in air. *Caution! Piranha solution is extremely corrosive and reacts violently with organic materials. It should be handled with great care.* SEM images were taken on a Philips XL30 instrument at an operation voltage of 15 kV. The SEM samples were prepared by placing a drop of the particle suspension onto a clean silicon wafer, followed by sputter-coating with gold. The zeta-potential of the particles was measured using a Zetasizer Nano-ZS instrument (Malvern Instruments, Malvern, UK). Particle counting and particle fluorescence measurements were performed by flow cytometry (Apogee Flow). Image analysis was conducted using ImageJ software.

Mechanical Property Measurements and Analysis. Mechanical property measurements of the PEG particles were conducted using a Nanowizard II atomic force microscope equipped with a fluorescence microscope (Lecia DMI4000B). The samples were prepared by placing a drop of concentrated AF488-labeled PEG particle suspension (approximately 10 μL) onto a PEI-precoated

FluoroDish (50 mm, World Precision Instruments Inc.), which was subsequently filled with Milli-Q water. A monolayer of PEG particles were immobilized at the base of the FluoroDish after settling and visualized by fluorescence microscopy (60× oil immersion objective). The probe used in this experiment was prepared by modifying the cantilever (MLCT, Bruker AFM Probes) by attaching a spherical glass bead (diameter = 22 μm, Polysciences) using an epoxy resin (Selleys Araldite Super Strength, Selleys) through micromanipulation in an AFM system (Figure S5a). After drying the glued glass bead overnight for complete curing, the resultant probe was thoroughly cleaned with ethanol, water, and *via* an oxygen plasma treatment. The spring constant of the probe was 0.09 N m^{-1} determined using the Hutter–Bechhoefer method.[65]

For the measurements, the probe was slowly lowered into an aqueous particle suspension avoiding air bubbles and hydrodynamic effects. A clean area on the glass with no particles was used for calibration. Next, the probe was slowly lowered onto individual immobilized particles ensuring vertical alignment by using the inbuilt micromanipulation stage. The location of individual particles was identified by fluorescence microscopy. Force measurements were performed at an approach velocity of 2 μm s^{-1} with a maximum indentation force of approximately 10 nN. Force–deformation curves were obtained from the raw AFM voltage–displacement data processed using JPK data processing software (v.4.4.29). After completing the measurements on a single particle, the location of the particle was assessed using the attached fluorescence microscope. The particle position remained unchanged during the measurements (Figure S5b and c). Six repeated measurements were performed for each particle, and at least five different particles were measured and analyzed for each sample to obtain representative Young's modulus values for the PEG particles.

The Hertz theory, which predicts force (F) on a particle as a function of a (small) applied indentation by a spherical probe, was used as follows:[66]

$$F = \frac{4E\sqrt{R_{\text{eff}}}}{3(1-\nu^2)}\delta^{3/2} \quad (2)$$

where $R_{\text{eff}} = \frac{RR_{\text{p}}}{R+R_{\text{p}}}$ is the effective radius of the probe radius R_{p} and the PEG hydrogel particle radius R. Equation (2) is valid when the Young's modulus of the indenter E_{p} is greater than the elastic modulus of the PEG hydrogel particle (E). Otherwise, the effective Young's modulus is used. In the present work, the probe is stiffer than the PEG hydrogel particle hence the equation is valid. Here, F is the force measured as a function of indentation of the probe into the particle (δ) and ν is the Poisson ratio (~0.4). The Young's modulus value of the PEG particles was evaluated from the linear range (δ from 0 to 200 nm) of the F–$\delta^{3/2}$ curves. The slope of the F–$\delta^{3/2}$ curves ($\frac{4E\sqrt{R_{\text{eff}}}}{3(1-\nu^2)}$) was used to calculate the modulus.

RAW264.7 Cell Association. RAW264.7 cells were seeded in a 24-well plate (80 000 cells per well) in RPMI media with 10% (v/v) FBS and treated with AF488-labeled MS@PEG$_{3\text{-arm}}$, MS@PEG$_{4\text{-arm}}$, MS@PEG$_{6\text{-arm}}$, MS@PEG$_{8\text{-arm}}$, or the corresponding PEG particles at a particle-to-cell ratio of 100:1 or 1000:1. After 12 or 24 h of incubation at 37 °C, the cells were detached from the plate using trypsin and subsequently washed with DPBS three times *via* centrifugation (300*g*, 5 min). The resultant cell pellets were resuspended in DPBS and analyzed by flow cytometry (Apogee Flow).

Confocal Microscopy Imaging of RAW264.7 Cell Association. RAW264.7 cells were seeded in a 8-well Lab-Tek chambered coverglass slides (Thermo Fisher Scientific, USA) (40 000 cells per well) in RPMI media with 10% (v/v) FBS and treated with AF488-labeled MS@PEG$_{3\text{-arm}}$, MS@PEG$_{4\text{-arm}}$, MS@PEG$_{6\text{-arm}}$, MS@PEG$_{8\text{-arm}}$ particles, or the corresponding PEG particles at a

particle-to-cell ratio of 100:1 for 12 h at 37 °C. After incubation, the cells were gently washed with DPBS and then fixed with paraformaldehyde (4% in DPBS) for 15 min at room temperature. The fixed cells were then stained with WGA-594 (5 μg mL^{-1}) for 5 min and Hoechst 33342 (0.1 mg mL^{-1}) for 5 min at room temperature. Cellular association imaging was performed using a Nikon A1R+ laser scanning confocal microscope (Nikon Corporation, Japan) equipped with a Plan Apo λ 60× 1.4 NA oil immersion objective, and 405, 488, 561, and 640 nm lasers, and analyzed by ImageJ software.

Immune Cell Association in Human Whole Blood. The human whole blood assay was conducted based on a modified previously developed method.[53] Fresh blood from a healthy volunteer was collected into sodium heparin vacuettes (Greiner Bio-One) and then aliquoted in 100 μL in polystyrene tubes (Falcon® Round-Bottom Polystyrene Tubes, 5 mL) with informed participant consent in accordance with the University of Melbourne Human ethics approval 1443420 and the Australian National Health and Medical Research Council Statement on Ethical Conduct in Human Research. Cell numbers were counted on a CELL-DYN Emerald analyzer (Abbott) using 20 μL of blood. The MS@PEG or PEG particles dispersed in DPBS (approximately 5 μL) were added to the blood and incubated for 1 h at 37 °C. The ratio of the particles to white blood cells (also called leukocytes) was 50:1, 20:1, 10:1, and 5:1 for the MS@PEG particles, and 200:1, 100:1, and 50:1 for the PEG particles. After incubation, the red blood cells were lysed using 4 mL of PharmLyse buffer and removed by centrifugation (500*g*, 5 min). After washing twice with 4 mL of DPBS (500*g*, 7 min), the cells were phenotyped on ice for 30 min using an antibody cocktail consisting of Lin-1 FITC, CD66b BV421 (G10F5), CD19 BUV395 (SJ25C1), CD3 AF700 (SP34-2), CD14 APC-H7 (MΦP9), CD56 PE (B159), and HLA-DR PE-CF594 (G46-6) in titrated concentrations. The cells were then washed twice with flow cytometry staining (FACS)

wash buffer (DPBS containing 2 mM EDTA and 0.5% w/v BSA, pH 8.0) and centrifuged at 500*g* for 7 min to remove free antibodies. After fixation, by adding 100 μL of 1% w/v formaldehyde, the cells were analyzed by flow cytometry (LSRFortessa, BD Biosciences). The data were analyzed using FlowJo V10.

Immune Cell Association in Washed Blood. The human washed blood assay was conducted based on a modified previously developed method.[51] Fresh blood collected from a healthy volunteer was centrifuged (900*g*, 15 min, no brake) in sodium heparin vacuettes (Greiner Bio-One) directly. The supernatant was collected and transferred into a 1.5 mL eppendorf tube for further centrifugation (1500*g*, 10 min) to remove any remaining cells, resulting in human plasma for the subsequent experiments. The blood cells remaining in the sodium heparin vacuettes were transferred into a 50 mL tube filled with DPBS, resuspended, and then centrifuged at 950*g* for 10 min with low brake. The supernatant was discarded, and this washing step was repeated for another four times until the absorbance of the supernatant at 280 nm was ~0 as measured using Nanodrop (Thermo Fisher Scientific, Australia), which confirmed the absence of plasma proteins. The cells were finally resuspended in DPBS in a cell concentration similar to that of whole blood (Table S4) and was termed as "washed blood". The concentrated MS@PEG or PEG particles were preincubated in 50 μL of DPBS or plasma for 1 h at 37 °C. The fluorescence intensity of particles with or without a biomolecular corona was monitored by flow cytometry (Figure S19). Approximately 5 μL of the above particle suspension was added to 100 μL of washed blood at a particle-to-cell ratio of 10:1 for the MS@PEG particles or 100:1 for the PEG particles. Subsequent steps were the same as those used in the human whole blood assay.

Formation of Biomolecular Corona-Coated Particles. MS@PEG and PEG particles (2×10^8 dispersed in DPBS) were incubated in 300 μL of plasma that was separated from human whole

blood for 1 h at 37 °C with constant shaking (600 rpm). The particles were then washed with DPBS six times resulting in "hard" corona-coated particles, directly used for zeta-potential measurements, SDS-PAGE analysis, and mass spectrometry analysis.

SDS-PAGE. The biomolecular corona-coated particles were obtained as described above. The adsorbed proteins were eluted from the particles by incubating the particles with NuPAGE LDS sample buffer and NuPAGE sample reducing agent, followed by heating to 70 °C for 10 min. After removal of the particles by centrifugation, the supernatant was loaded on 4–20% Mini-PROTEAN TGX gel (BioRad) running at 120 V for 40 min. Diluted plasma was also loaded as control. After washing with reverse osmosis (RO) water, the gel was stained with SimplyBlue overnight, and rinsed with RO water three times prior to imaging.

Proteomics Analysis by Mass Spectrometry. Samples for mass spectrometry analysis were prepared following a standard protocol. Briefly, the biomolecular corona-coated particles were incubated in a mixture of 25 µL of 100 mM TEAB, 25 µL of TFE, and 2.5 µL of 200 mM TCEP at 60 °C for 45 min for protein denaturation. Then, 10 µL of 200 mM IAM (in 50 mM TEAB) was added to the mixture, followed by incubation for 45 min at room temperature in the dark. Then, 2.5 µL of 200 mM TCEP was added to the mixture for incubation for 30 min at room temperature in the dark to remove excess IAM. The mixture was subsequently diluted by adding 300 µL of water and the pH was raised to between 7.5 and 8.0 by adding 100 µL of 100 mM TEAB. The eluted proteins were digested by incubating with 0.2 µg of trypsin overnight at 37 °C. The trypsin activity was stopped by adding 2 µL of formic acid to lower the pH. The resultant mixture was centrifuged at 15000*g* for 10 min to remove any pellets. The collected supernatant was freeze-dried followed by resuspending in 20 µL of 2% CH_3CN/0.05% TFA.

Three replicates of each samples were analyzed by LC-MS/MS using a Q Exactive Plus Orbitrap mass spectrometer (Thermo Scientific) with a nanoESI interface in conjunction with an Ultimate 3000 RSLC nanoHPLC (Dionex Ultimate 3000). The LC system was equipped with an Acclaim PepMap nano-trap column (Dinoex-C18, 100 Å, 75 µm × 2 cm) and an Acclaim PepMap RSLC analytical column (Dinoex-C18, 100 Å, 75 µm × 50 cm). The tryptic peptides were injected to the enrichment column at an isocratic flow of 5 µL min^{-1} of 2% v/v CH_3CN containing 0.1% v/v formic acid for 5 min applied before the enrichment column was switched in-line with the analytical column. The eluents were 0.1% v/v formic acid (solvent A) and 100% v/v CH_3CN in 0.1% v/v formic acid (solvent B). The flow gradient was (i) 0–6min at 3% B, (ii) 6–40 min at 3–25% B, (iii) 40–48 min at 25–45% B, (iv) 48–50 min at 40–80% B, (v) 50–53 min at 85–85% B, (vi) 53–54 min at 85–3% and equilibrated at 3% B for 10 min before the next sample injection. The Q Exactive Plus mass spectrometer was operated in the data-dependent mode, whereby full MS1 spectra were acquired in positive mode, 70 000 resolution, automatic gain control (AGC) target of $3e^6$, and maximum accumulation time of 50 ms. Fifteen of the most intense peptide ions with charge states ≥2 and intensity threshold of $1.7e^4$ were isolated for MS/MS. The isolation window was set at 1.2 *m*/*z* and precursors fragmented using normalized collision energy of 30 at 17 500 resolution, AGC target of $1e^5$, and maximum accumulation time of 100 ms. Dynamic exclusion was set to be 30 s.

Raw files were processed using the MaxQuant platform (version 1.6.10.43) and searched against UniProt human database (January 2019) using default settings for Orbitrap instrument.[67] Trypsin was selected as the enzyme with the number of maximum missed cleavages set to two. Fixed modification was carbamidomethyl of cysteine, whereas variable modifications included acetyl (protein *N*-terminus) and oxidation of methionine. False discovery rate was set to 1% on both

protein and peptide level. LFQ required a minimum of two peptides with at least one razor or unique peptide. Protein groups identified in MaxQuant were imported into Perseus for further analysis.[68] Three replicates of each sample were analyzed and only proteins that were identified in at least two replicates were evaluated for abundance. The heat map (Figure 6a) plotted by GraphPad Prism 7.00 was generated from the average values of $\log_2$(LFQ) for each identified protein from three independent experimental replicates. The protein contents (mol% of total proteins) for semi-quantitative assessment of protein abundance were calculated using Equation (3):

$$\mathrm{mol\%_A} = \frac{\mathrm{iBAQ_A}}{\mathrm{iBAQ_{sum}}} \tag{3}$$

where $\mathrm{mol\%_A}$ is the content of protein A, $\mathrm{iBAQ_A}$ is the intensity-based absolute quantification value of protein A, and $\mathrm{iBAQ_{sum}}$ is the sum of iBAQ values of all the identified proteins.[69–71]

As the same number of particles was employed for the mass spectrometry analysis for each sample, comparison of total protein adsorption on different MS@PEG and PEG particles can be performed from the sum of iBAQ values of all the adsorbed proteins as shown in Figure 6b,[72] wherein the sum iBAQ value of the $\mathrm{MS@PEG_{3\text{-}arm}}$ particles was normalized as 100% and that of the other particles was expressed as a percentage relative to the $\mathrm{MS@PEG_{3\text{-}arm}}$ particles. The Pearson correlation analysis between the functional proteins and cellular association was conducted by GraphPad Prism 7.00.

Statistical Analysis. Statistical analysis was conducted using GraphPad Prism 7.00 software. Statistical significance was determined by using one-way analysis of variance (ANOVA) or two-way ANOVA. Non-significant (ns) $p > 0.05$, * $p < 0.05$, ** $p < 0.01$, *** $p < 0.001$, **** $p < 0.0001$. The specific statistical test performed for each experiment is included in the figure legends.

Minimum Information Reporting in Bio–Nano Experimental Literature (MIRIBEL). The studies conducted herein, including material characterization, biological characterization, and experimental details, conform to the MIRIBEL reporting standard for bio–nano research,[73] and we include a companion checklist of these components in the Supporting Information.

ASSOCIATED CONTENT

Supporting Information. Molecular structures of 3-arm-PEG-NH_2, 4-arm-PEG-NH_2, 6-arm-PEG-NH_2, 8-arm-PEG-NH_2, and 8-arm-PEG-NHS, MS particle characterization, AFM images and corresponding height profiles of PEG particles, fluorescence microscopy images of PEG particles and optical microscopy image of the silica colloidal probe for CP-AFM force measurements, TEM images of MS@PEG particles, RAW264.7 cell association and imaging, gating method for human blood assays, cellular association with NK cells, T cells, and dendritic cells, zeta-potential measurements, statistical analysis of cellular association, SDS-PAGE analysis, statistical analysis of total protein adsorption on different particles, particle fluorescence intensity distribution, fluorescence intensity distributions of AF647 negative and AF647 positive cells by flow cytometry, full lists of the proteins identified by mass spectrometry, cell count data and antibody details of human blood assays, and MIRIBEL checklist for reporting research in bio–nano science.

AUTHOR INFORMATION

Corresponding Author

*E-mail: skent@unimelb.edu.au.

*E-mail: fcaruso@unimelb.edu.au.

Notes

The authors declare no competing interests.

ACKNOWLEDGMENT

This research was conducted and funded by the Australian Research Council Centre of Excellence in Convergent Bio-Nano Science and Technology (project number CE140100036). F.C. and S.J.K acknowledge the award of a National Health and Medical Research Council Senior Principal Research Fellowship (GNT1135806 and GNT1136322, respectively). This work was performed in part at the Materials Characterisation and Fabrication Platform (MCFP) and the Biosciences Microscopy Facility at The University of Melbourne, the Victorian Node of the Australian National Fabrication Facility (ANFF), and the Peter Doherty Institute. We acknowledge Y. Qu and Y. Han for assistance with experiments, and H. G. Kelly and M. Faria for helpful discussions.

REFERENCES

(1) Langer, R. New Methods of Drug Delivery. *Science* **1990**, *249*, 1527–1533.

(2) Otsuka, H.; Nagasaki, Y.; Kataoka, K. PEGylated Nanoparticles for Biological and Pharmaceutical Applications. *Adv. Drug Delivery Rev.* **2003**, *55*, 403–419.

(3) Mitragotri, S.; Burke, P. A.; Langer, R. Overcoming the Challenges in Administering Biopharmaceuticals: Formulation and Delivery Strategies. *Nat. Rev. Drug Discovery* **2014**, *13*, 655–672.

(4) Cui, J.; Richardson, J. J.; Bjornmalm, M.; Faria, M.; Caruso, F. Nanoengineered Templated Polymer Particles: Navigating the Biological Realm. *Acc. Chem. Res.* **2016**, *49*, 1139–1148.

(5) Zelikin, A. N.; Ehrhardt, C.; Healy, A. M. Materials and Methods for Delivery of Biological Drugs. *Nat. Chem.* **2016**, *8*, 997–1007.

(6) Tibbitt, M. W.; Dahlman, J. E.; Langer, R. Emerging Frontiers in Drug Delivery. *J. Am. Chem. Soc.* **2016**, *138*, 704–717.

(7) Patra, J. K.; Das, G.; Fraceto, L. F.; Campos, E. V. R.; Rodriguez-Torres, M. D. P.; Acosta-Torres, L. S.; Diaz-Torres, L. A.; Grillo, R.; Swamy, M. K.; Sharma, S.; Habtemariam, S.; Shin, H.-S. Nano Based Drug Delivery Systems: Recent Developments and Future Prospects. *J. Nanobiotechnol.* **2018**, *16*, 71.

(8) Albanese, A.; Tang, P. S.; Chan, W. C. The Effect of Nanoparticle Size, Shape, and Surface Chemistry on Biological Systems. *Annu. Rev. Biomed. Eng.* **2012**, *14*, 1–16.

(9) Walkey, C. D.; Olsen, J. B.; Guo, H.; Emili, A.; Chan, W. C. Nanoparticle Size and Surface Chemistry Determine Serum Protein Adsorption and Macrophage Uptake. *J. Am. Chem. Soc.* **2012**, *134*, 2139–2147.

(10) Jiang, Y.; Huo, S.; Mizuhara, T.; Das, R.; Lee, Y. W.; Hou, S.; Moyano, D. F.; Duncan, B.; Liang, X. J.; Rotello, V. M. The Interplay of Size and Surface Functionality on the Cellular Uptake of Sub-10 nm Gold Nanoparticles. *ACS Nano* **2015**, *9*, 9986–9993.

(11) Song, D.; Cui, J.; Ju, Y.; Faria, M.; Sun, H.; Howard, C. B.; Thurecht, K. J.; Caruso, F. Cellular Targeting of Bispecific Antibody-Functionalized Poly(ethylene Glycol) Capsules: Do Shape and Size Matter? *ACS Appl. Mater. Interfaces* **2019**, *11*, 28720–28731.

(12) Anselmo, A. C.; Zhang, M.; Kumar, S.; Vogus, D. R.; Menegatti, S.; Helgeson, M. E.; Mitragotri, S. Elasticity of Nanoparticles Influences Their Blood Circulation, Phagocytosis, Endocytosis, and Targeting. *ACS Nano* **2015**, *9*, 3169–3177.

(13) Saha, K.; Rahimi, M.; Yazdani, M.; Kim, S. T.; Moyano, D. F.; Hou, S.; Das, R.; Mout, R.; Rezaee, F.; Mahmoudi, M. Rotello, V. M. Regulation of Macrophage Recognition through the Interplay of Nanoparticle Surface Functionality and Protein Corona. *ACS Nano* **2016**, *10*, 4421–4430.

(14) Baimanov, D.; Cai, R.; Chen, C. Understanding the Chemical Nature of Nanoparticle–Protein Interactions. *Bioconjugate Chem.* **2019**, *30*, 1923–1937.

(15) Giulimondi, F.; Digiacomo, L.; Pozzi, D.; Palchetti, S.; Vulpis, E.; Capriotti, A. L.; Chiozzi, R. Z.; Lagana, A.; Amenitsch, H.; Masuelli, L.; Peruzzi, G.; Mahmoudi, M.; Screpanti, I.; Zingoni, A.; Caracciolo, G. Interplay of Protein Corona and Immune Cells Controls Blood Residency of Liposomes. *Nat. Commun.* **2019**, *10*, 3686.

(16) Walkey, C. D.; Chan, W. C. Understanding and Controlling the Interaction of Nanomaterials with Proteins in a Physiological Environment. *Chem. Soc. Rev.* **2012**, *41*, 2780–2799.

(17) Lundqvist, M.; Stigler, J.; Elia, G.; Lynch, I.; Cedervall, T.; Dawson, K. A. Nanoparticle Size and Surface Properties Determine the Protein Corona with Possible Implications for Biological Impacts. *Proc. Natl. Acad. Sci. U. S. A.* **2008**, *105*, 14265–14270.

(18) Caracciolo, G.; Farokhzad, O. C.; Mahmoudi, M. Biological Identity of Nanoparticles *in Vivo*: Clinical Implications of the Protein Corona. *Trends Biotechnol.* **2017**, *35*, 257–264.

(19) Hadjidemetriou, M.; McAdam, S.; Garner, G.; Thackeray, C.; Knight, D.; Smith, D.; Al-Ahmady, Z.; Mazza, M.; Rogan, J.; Clamp, A.; Kostarelos, K. The Human *in Vivo* Biomolecule Corona onto PEGylated Liposomes: A Proof-of-Concept Clinical Study. *Adv. Mater.* **2019**, *31*, e1803335.

(20) Khongkow, M.; Yata, T.; Boonrungsiman, S.; Ruktanonchai, U. R.; Graham, D.; Namdee, K. Surface Modification of Gold Nanoparticles with Neuron-Targeted Exosome for Enhanced Blood–Brain Barrier Penetration. *Sci. Rep.* **2019**, *9*, 8278.

(21) Dobrovolskaia, M. A.; McNeil, S. E. Immunological Properties of Engineered Nanomaterials. *Nat. Nanotechnol.* **2007**, *2*, 469–478.

(22) Garcia, I.; Sanchez-Iglesias, A.; Henriksen-Lacey, M.; Grzelczak, M.; Penades, S.; Liz-Marzan, L. M. Glycans as Biofunctional Ligands for Gold Nanorods: Stability and Targeting in Protein-Rich Media. *J. Am. Chem. Soc.* **2015**, *137*, 3686–3692.

(23) Wang, J.; Yue, Y.; Chen, G.; Xia, J. Protease-Promoted Drug Delivery Using Peptide-Functionalized Gold Nanoparticles. *Soft Matter* **2011**, *7*, 7217–7222.

(24) Vargas, K. M.; Shon, Y. S. Hybrid Lipid–Nanoparticle Complexes for Biomedical Applications. *J. Mater. Chem. B* **2019**, *7*, 695–708.

(25) Pombo Garcia, K.; Zarschler, K.; Barbaro, L.; Barreto, J. A.; O'Malley, W.; Spiccia, L.; Stephan, H.; Graham, B. Zwitterionic-Coated "Stealth" Nanoparticles for Biomedical Applications: Recent Advances in Countering Biomolecular Corona Formation and Uptake by the Mononuclear Phagocyte System. *Small* **2014**, *10*, 2516–2529.

(26) Suk, J. S.; Xu, Q.; Kim, N.; Hanes, J.; Ensign, L. M. PEGylation as a Strategy for Improving Nanoparticle-Based Drug and Gene Delivery. *Adv. Drug Delivery Rev.* **2016**, *99*, 28–51.

(27) Pelaz, B.; del Pino, P.; Maffre, P.; Hartmann, R.; Gallego, M.; Rivera-Fernandez, S.; de la Fuente, J. M.; Nienhaus, G. U.; Parak, W. J. Surface Functionalization of Nanoparticles with Polyethylene Glycol: Effects on Protein Adsorption and Cellular Uptake. *ACS Nano* **2015**, *9*, 6996–7008.

(28) Kolate, A.; Baradia, D.; Patil, S.; Vhora, I.; Kore, G.; Misra, A. PEG – A Versatile Conjugating Ligand for Drugs and Drug Delivery Systems. *J. Controlled Release* **2014**, *192*, 67–81.

(29) Gustafson, H. H.; Holt-Casper, D.; Grainger, D. W.; Ghandehari, H. Nanoparticle Uptake: The Phagocyte Problem. *Nano Today* **2015**, *10*, 487–510.

(30) Xu, Q.; Ensign, L. M.; Boylan, N. J.; Schon, A.; Gong, X.; Yang, J. C.; Lamb, N. W.; Cai, S.; Yu, T.; Freire, E.; Hanes, J. Impact of Surface Polyethylene Glycol (PEG) Density on Biodegradable Nanoparticle Transport in Mucus *ex Vivo* and Distribution *in Vivo*. *ACS Nano* **2015**, *9*, 9217–9227.

(31) Zhang, P.; Zhang, Z.; Wang, D.; Hao, J.; Cui, J. Monodispersity of Poly(ethylene Glycol) Matters for Low-Fouling Coatings. *ACS Macro Lett.* **2020**, *9*, 1478–1482.

(32) Gref, R.; Luck, M.; Quellec, P.; Marchand, M.; Dellacherie, E.; Harnisch, S.; Blunk, T.; Muller, R. H. “Stealth” Corona-Core Nanoparticles Surface Modified by Polyethylene Glycol (PEG): Influences of the Corona (PEG Chain Length and Surface Density) and of the Core

Composition on Phagocytic Uptake and Plasma Protein Adsorption. *Colloids Surf., B. Biointerfaces* **2000**, *18*, 301–313.

(33) Cruz, L. J.; Tacken, P. J.; Fokkink, R.; Figdor, C. G. The Influence of PEG Chain Length and Targeting Moiety on Antibody-Mediated Delivery of Nanoparticle Vaccines to Human Dendritic Cells. *Biomaterials* **2011**, *32*, 6791–6803.

(34) Xu, J.; Wong, D. H.; Byrne, J. D.; Chen, K.; Bowerman, C.; DeSimone, J. M. Future of the Particle Replication in Nonwetting Templates (PRINT) Technology. *Angew. Chem. Int. Ed.* **2013**, *52*, 6580–6589.

(35) Dendukuri, D.; Pregibon, D. C.; Collins, J.; Hatton, T. A.; Doyle, P. S. Continuous-Flow Lithography for High-Throughput Microparticle Synthesis. *Nat. Mater.* **2006**, *5*, 365–369.

(36) Yap, H. P.; Johnston, A. P.; Such, G. K.; Yan, Y.; Caruso, F. Click-Engineered, Bioresponsive, Drug-Loaded PEG Spheres. *Adv. Mater.* **2009**, *21*, 4348–4352.

(37) Leung, M. K.; Such, G. K.; Johnston, A. P.; Biswas, D. P.; Zhu, Z.; Yan, Y.; Lutz, J. F.; Caruso, F. Assembly and Degradation of Low-Fouling Click-Functionalized Poly(ethylene Glycol)-Based Multilayer Films and Capsules. *Small* **2011**, *7*, 1075–1085.

(38) Gao, Z.; Zhu, H.; Li, X.; Zhang, P.; Ashokkumar, M.; Cavalieri, F.; Hao, J.; Cui, J. Sono-Polymerization of Poly(ethylene Glycol)-Based Nanoparticles for Targeted Drug Delivery. *ACS Macro Lett.* **2019**, *8*, 1285–1290.

(39) Cui, J.; Bjornmalm, M.; Liang, K.; Xu, C.; Best, J. P.; Zhang, X.; Caruso, F. Super-Soft Hydrogel Particles with Tunable Elasticity in a Microfluidic Blood Capillary Model. *Adv. Mater.* **2014**, *26*, 7295–7299.

(40) Cui, J.; De Rose, R.; Alt, K.; Alcantara, S.; Paterson, B. M.; Liang, K.; Hu, M.; Richardson, J. J.; Yan, Y.; Jeffery, C. M.; Price, R. I.; Peter, K.; Hagemeyer, C. E.; Donnelly, P. S.; Kent, S. J.; Caruso, F. Engineering Poly(ethylene Glycol) Particles for Improved Biodistribution. *ACS Nano* **2015**, *9*, 1571–1580.

(41) Cui, J.; Ju, Y.; Houston, Z. H.; Glass, J. J.; Fletcher, N. L.; Alcantara, S.; Dai, Q.; Howard, C. B.; Mahler, S. M.; Wheatley, A. K. Modulating Targeting of Poly(ethylene Glycol) Particles to Tumor Cells Using Bispecific Antibodies. *Adv. Healthcare Mater.* **2019**, *8*, 1801607.

(42) Cui, J.; Alt, K.; Ju, Y.; Gunawan, S. T.; Braunger, J. A.; Wang, T. Y.; Dai, Y.; Dai, Q.; Richardson, J. J.; Guo, J.; Björnmalm, M.; Hagemeyer, C. E.; Caruso, F. Ligand-Functionalized Poly(ethylene Glycol) Particles for Tumor Targeting and Intracellular Uptake. *Biomacromolecules* **2019**, *20*, 3592–3600.

(43) Cui, J.; Bjornmalm, M.; Ju, Y.; Caruso, F. Nanoengineering of Poly(ethylene Glycol) Particles for Stealth and Targeting. *Langmuir* **2018**, *34*, 10817–10827.

(44) Ju, Y.; Cui, J.; Mullner, M.; Suma, T.; Hu, M.; Caruso, F. Engineering Low-Fouling and pH-Degradable Capsules through the Assembly of Metal–Phenolic Networks. *Biomacromolecules* **2015**, *16*, 807–814.

(45) Tan, H.; Wang, W.; Yu, C.; Zhou, Y.; Lu, Z.; Yan, D. Dissipative Particle Dynamics Simulation Study on Self-Assembly of Amphiphilic Hyperbranched Multiarm Copolymers with Different Degrees of Branching. *Soft Matter* **2015**, *11*, 8460–8470.

(46) Kadlecova, Z.; Rajendra, Y.; Matasci, M.; Baldi, L.; Hacker, D. L.; Wurm, F. M.; Klok, H. A. DNA Delivery with Hyperbranched Polylysine: A Comparative Study with Linear and Dendritic Polylysine. *J. Controlled Release* **2013**, *169*, 276–288.

(47) Cook, A. B.; Perrier, S. Branched and Dendritic Polymer Architectures: Functional Nanomaterials for Therapeutic Delivery. *Adv. Funct. Mater.* **2020**, *30*, 1901001.

(48) Laskowski, Ł.; Laskowska, M.; Vila, N.; Schabikowski, M.; Walcarius, A. Mesoporous Silica-Based Materials for Electronics-Oriented Applications. *Molecules* **2019**, *24*, 2395.

(49) Langhans, S. A. Three-Dimensional *in Vitro* Cell Culture Models in Drug Discovery and Drug Repositioning. *Front. Pharmacol.* **2018**, *9*, 6.

(50) Sathyamoorthy, N.; Dhanaraju, M. D. Shielding Therapeutic Drug Carriers from the Mononuclear Phagocyte System: A Review. *Crit. Rev. Ther. Drug Carrier Syst.* **2016**, *33*, 489–567.

(51) Weiss, A. C. G.; Kelly, H. G.; Faria, M.; Besford, Q. A.; Wheatley, A. K.; Ang, C. S.; Crampin, E. J.; Caruso, F.; Kent, S. J. Link between Low-Fouling and Stealth: A Whole Blood Biomolecular Corona and Cellular Association Analysis on Nanoengineered Particles. *ACS Nano* **2019**, *13*, 4980–4991.

(52) Ju, Y.; Kelly, H. G.; Dagley, L. F.; Reynaldi, A.; Schlub, T. E.; Spall, S. K.; Bell, C. A.; Cui, J.; Mitchell, A. J.; Lin, Z.; Wheatley, A. K.; Thurecht, K. J.; Davenport, M. P.; Webb, A. I.; Caruso, F.; Kent, S. J. Person-Specific Biomolecular Coronas Modulate Nanoparticle Interactions with Immune Cells in Human Blood. *ACS Nano* **2020**, *14*, 15723.

(53) Glass, J. J.; Li, Y.; De Rose, R.; Johnston, A. P.; Czuba, E. I.; Khor, S. Y.; Quinn, J. F.; Whittaker, M. R.; Davis, T. P.; Kent, S. J. Thiol-Reactive Star Polymers Display Enhanced Association with Distinct Human Blood Components. *ACS Appl. Mater. Interfaces* **2017**, *9*, 12182–12194.

(54) Hui, Y.; Yi, X.; Hou, F.; Wibowo, D.; Zhang, F.; Zhao, D. Y.; Gao, H. J.; Zhao, C. X. Role of Nanoparticle Mechanical Properties in Cancer Drug Delivery. *ACS Nano* **2019**, *13*, 7410–7424.

(55) Zhang, L.; Cao, Z.; Li, Y.; Ella-Menye, J. R.; Bai, T.; Jiang, S. Softer Zwitterionic Nanogels for Longer Circulation and Lower Splenic Accumulation. *ACS Nano* **2012**, *6*, 6681–6686.

(56) Banquy, X.; Suarez, F.; Argaw, A.; Rabanel, J.-M.; Grutter, P.; Bouchard, J.-F.; Hildgen, P.; Giasson, S. Effect of Mechanical Properties of Hydrogel Nanoparticles on Macrophage Cell Uptake. *Soft Matter* **2009**, *5*, 3984–3991.

(57) Anselmo, A. C.; Mitragotri, S. Impact of Particle Elasticity on Particle-Based Drug Delivery Systems. *Adv. Drug Delivery Rev.* **2017**, *108*, 51–67.

(58) Cacopardo, L.; Mattei, G.; Ahluwalia, A. A New Load-Controlled Testing Method for Viscoelastic Characterisation through Stress-Rate Measurements. *Materialia* **2020**, *9*, 100552.

(59) Monopoli, M. P.; Aberg, C.; Salvati, A.; Dawson, K. A. Biomolecular Coronas Provide the Biological Identity of Nanosized Materials. *Nat. Nanotechnol.* **2012**, *7*, 779–786.

(60) Unsworth, L. D.; Sheardown, H.; Brash, J. L. Protein-Resistant Poly(ethylene Oxide)-Grafted Surfaces: Chain Density-Dependent Multiple Mechanisms of Action. *Langmuir* **2008**, *24*, 1924–1929.

(61) Penna, M. J.; Mijajlovic, M.; Biggs, M. J. Molecular-Level Understanding of Protein Adsorption at the Interface between Water and a Strongly Interacting Uncharged Solid Surface. *J. Am. Chem. Soc.* **2014**, *136*, 5323–5331.

(62) Poon, I. K.; Patel, K. K.; Davis, D. S.; Parish, C. R.; Hulett, M. D. Histidine-Rich Glycoprotein: The Swiss Army Knife of Mammalian Plasma. *Blood* **2011**, *117*, 2093–2101.

(63) Fedeli, C.; Segat, D.; Tavano, R.; Bubacco, L.; De Franceschi, G.; de Laureto, P. P.; Lubian, E.; Selvestrel, F.; Mancin, F.; Papini, E. The Functional Dissection of the Plasma Corona of SiO_2-NPs Spots Histidine Rich Glycoprotein as a Major Player Able to Hamper Nanoparticle Capture by Macrophages. *Nanoscale* **2015**, *7*, 17710–17728.

(64) Jones, A. L.; Hulett, M. D.; Parish, C. R. Histidine-Rich Glycoprotein: A Novel Adaptor Protein in Plasma That Modulates the Immune, Vascular and Coagulation Systems. *Immunol. Cell Biol.* **2005**, *83*, 106–118.

(65) Hutter, J. L.; Bechhoefer, J. Calibration of Atomic-Force Microscope Tips. *Rev. Sci. Instrum.* **1993**, *64*, 1868–1873.

(66) Hertz, H. Ueber Die Berührung Fester Elastischer Körper. *J. Reine Angew. Math.* **1882**, *1882*, 156–171.

(67) Tyanova, S.; Temu, T.; Cox, J. The MaxQuant Computational Platform for Mass Spectrometry-Based Shotgun Proteomics. *Nat. Protoc.* **2016**, *11*, 2301–2319.

(68) Tyanova, S.; Temu, T.; Sinitcyn, P.; Carlson, A.; Hein, M. Y.; Geiger, T.; Mann, M.; Cox, J. The Perseus Computational Platform for Comprehensive Analysis of (Prote)omics Data. *Nat. Methods* **2016**, *13*, 731–740.

(69) Zeng, X.; Sun, J.; Li, S.; Shi, J.; Gao, H.; Leong, W. S.; Wu, Y.; Li, M.; Liu, C.; Li, P. Blood-Triggered Generation of Platinum Nanoparticle Functions as an Anti-Cancer Agent. *Nat. Commun.* **2020**, *11*, 567.

(70) Schwanhausser, B.; Busse, D.; Li, N.; Dittmar, G.; Schuchhardt, J.; Wolf, J.; Chen, W.; Selbach, M. Global Quantification of Mammalian Gene Expression Control. *Nature* **2011**, *473*, 337–342.

(71) Saltzman, A. B.; Leng, M.; Bhatt, B.; Singh, P.; Chan, D. W.; Dobrolecki, L.; Chandrasekaran, H.; Choi, J. M.; Jain, A.; Jung, S. Y. gpGrouper: A Peptide Grouping Algorithm for Gene-Centric Inference and Quantitation of Bottom-Up Proteomics Data. *Mol. Cell. Proteomics* **2018**, *17*, 2270–2283.

(72) Zou, Y.; Ito, S.; Yoshino, F.; Suzuki, Y.; Zhao, L.; Komatsu, N. Polyglycerol Grafting Shields Nanoparticles from Protein Corona Formation to Avoid Macrophage Uptake. *ACS Nano* **2020**, *14*, 7216–7226.

(73) Faria, M.; Björnmalm, M.; Thurecht, K. J.; Kent, S. J.; Parton, R. G.; Kavallaris, M.; Johnston, A. P.; Gooding, J. J.; Corrie, S. R.; Boyd, B. J. Minimum Information Reporting in Bio–Nano Experimental Literature. *Nat. Nanotechnol.* **2018**, *13*, 777–785.

Table of Contents graphic